Journal of Marine Science and Technology

Volume 23 | Issue 6 Article 3

VISCOUS FLOW FIELDS INDUCED BY A BREAKING SOLITARY WAVE OVER A SHELF

Ching-Jer Huang
Department of Hydraulic and Ocean Engineering, National Cheng Kung University, Tainan, Taiwan, R.O.C. Coastal Ocean Monitoring Center, National Cheng Kung University, Tainan, Taiwan, R.O.C., cjhuang@mail.ncku.edu.tw

Yen-Tsen Lin
Department of Hydraulic and Ocean Engineering, National Cheng Kung University, Tainan, Taiwan, R.O.C.

Chun-Yuan Lin
Coastal Ocean Monitoring Center, National Cheng Kung University, Tainan, Taiwan, R.O.C.

VISCOUS FLOW FIELDS INDUCED BY A BREAKING SOLITARY WAVE OVER A SHELF

Acknowledgements

The authors would like to thank the National Science Council, Taiwan, for financially supporting this research under Contract No. NSC98-2221-E-006-252 -MY3

Journal of Marine Science and Technology, Vol. 23, No. 6, pp. 855-863 (2015)
DOI: 10.6119/JMST-015-0610-2

VISCOUS FLOW FIELDS INDUCED BY A BREAKING SOLITARY WAVE OVER A SHELF

Ching-Jer Huang[1, 2], Yen-Tsen Lin[1], and Chun-Yuan Lin[2]

Key words: RANS equations, particle level set method, solitary wave, splash-up, energy balance.

ABSTRACT

This work investigates the viscous flow fields induced by a solitary wave passing over a shelf or a step. The proposed numerical model solves the unsteady two-dimensional Reynolds Averaged Navier-Stokes (RANS) equations and the turbulence equations. The finite-analytical scheme is used to discretize the differential equations involved in the RANS model. The particle level set method is adopted to capture the complex free surface evolution. Accuracy of the proposed model in simulating breaking solitary wave on a shelf is verified by comparing numerical wave profiles from the incident stage to the beginning of jet fall with the experimental data. Following verification of the accuracy of the proposed numerical model, the surface evolution, kinematic properties and energy balance involved in a breaking solitary wave on the shelf are elucidated in details. Numerical results indicate that during the overturning of the solitary wave, maximum velocity of the fluid particles occurs after the first splash-up and before the second reattachment.

I. INTRODUCTION

Wave breaking is one of the most commonly observed features of water waves in the coastal zones. When waves break, the momentum of waves is transformed into the ocean surface layer. Wave breaking thus plays a significant role in the dissipation of wave energy. Given the high complexity of the phenomena associated with wave breaking, earlier research focused mainly on the evolution of a breaking solitary wave on a continental shelf, which is represented by a vertical step. Goring (1978) studied the reflection and transmission of a solitary wave passing over a shelf and the results were confirmed by experimental data. Losada et al. (1989) measured the evolution of a solitary wave at a step and classified the evolutions into four modes concerned mainly with the distortion, fission and breaking of the wave. Yasuda et al. (1997) investigated the kinematic properties of overturning solitary waves on a step by using the potential flow model. Surface profiles and velocity fields of the flow from the initial state to the state when the jets that are ejected from their crests plunge into the front faces were examined. Experiments were also performed to verify the accuracy of the numerical results for the temporal water surface elevation before the breaking point and the spatial water surface profiles around the ejected jet. Despite its contributions, their study did not address the surface evolution of the breaking solitary wave after the formation of the ejected jet, such as re-attachment, splash-up and air entrainment. By solving the Reynolds averaged Navier-Stokes (RANS) equations, Liu and Cheng (2001) studied the evolution of a solitary wave over a shelf. Both nonbreaking and breaking solitary waves were examined. The breaking waves were simulated by coupling the RANS equations with $k - \varepsilon$ turbulence equations. According to their numerical results, the fission processes for generating the second and third solitons are quite different for nonbreaking and breaking solitary waves.

The aforementioned research focuses mainly on the surface evolution of the breaking solitary waves. However, the kinematic behavior and energy balance of the flows associated with breaking waves are also crucial for elucidating the mechanism of the breaking waves. Many experimental studies have explored the kinematic behavior associated with breaking waves. By using the Particle Image Velocimetry technique, Chang and Liu (1998) measured the fluid particle velocities in the overturning jet of a breaking wave. According to their results, the maximum fluid particle velocity at the tip of the overturning jet reached 1.68 times of the phase velocity calculated from the linear wave theory.

The complicated free surfaces involved in a breaking wave have been simulated using numerical approaches such as the VOF method and the smoothed particle hydrodynamics (SPH) method. Recently, a level set method (LSM) is developed to capture the interface between two fluids. The level set method provides an effective means of computing the interface separation and combination, such as the motion of air bubbles in water or falling water drops in air. However, numerical dif-

Paper submitted 12/02/14; revised 01/28/15; accepted 06/10/15. Author for correspondence: Ching-Jer Huang (e-mail: cjhuang@mail.ncku.edu.tw).
[1] Department of Hydraulic and Ocean Engineering, National Cheng Kung University, Tainan, Taiwan, R.O.C.
[2] Coastal Ocean Monitoring Center, National Cheng Kung University, Tainan, Taiwan, R.O.C.

fusion may occur as time proceeds, subsequently affecting the correct capturing of the interface. Numerous studies have developed a more accurate and efficient solution algorithm, referred to as the particle level set method, to capture the interface accurately, subsequently improving the conservation of mass in the flow domain (Enright et al., 2002).

Wang et al. (2009) developed a two phase flow model to simulate spilling breaking waves, in which the level set method was implemented for retrieving the air-water interface. According to their results, surface elevation, location of the breaking point and undertow profiles can be captured. Lubin et al. (2011) simulated two-dimensional breaking waves over a sloping beach by solving the Navier-Stokes equations, in air and water, coupled with the large eddy simulation (LES). Their numerical results were compared with the experimental observations.

This work develops a numerical model to examine the surface evolution, kinematic properties, and energy balance involved in a breaking solitary wave over a shelf. The numerical model solves the unsteady, two-dimensional Reynolds Averaged Navier-Stokes (RANS) equations and the turbulence equations. The interface between the air and water phases was captured using the particle level set method.

II. GOVERNING EQUATIONS

This work develops a numerical model to study the surface evolution and kinematic behavior involved in a breaking solitary wave on a continental shelf. The continental shelf is represented by a step with a vertical face installed in the computational domain. For an incompressible, viscous fluid, the continuity equation in the Cartesian coordinate system is written in tensor form as

$$\frac{\partial U_i}{\partial x_i} = O \tag{1}$$

and the unsteady Reynolds Averaged Navier-Stokes (RANS) equations are

$$\frac{\partial U_i}{\partial t} + U_j \frac{\partial U_i}{\partial x_j} = -\frac{1}{\rho}\frac{\partial P}{\partial x_i} + \upsilon\left(\frac{\partial^2 U_i}{\partial x_j \partial x_j}\right) - \frac{\partial(\overline{u_i' u_j'})}{\partial x_j} \tag{2}$$

where U_i denotes time-averaged mean velocity of the fluid, for two-dimensional flows i ranges from 1 to 2; x_i is the coordinates; t is time; ρ is density; P is hydrodynamic pressure, which equals the reduction of the hydrostatic pressure from the total pressure, and $-\rho\overline{u_i' u_j'}$ are the Reynolds stress tensor.

In the $k-\varepsilon$ model of turbulent fluid flows, each Reynolds stress is related to the corresponding mean rates of strain by an isotropic eddy viscosity υ_T as follows:

$$-\overline{u_i' u_j'} = \upsilon_T\left(\frac{\partial U_i}{\partial x_j} + \frac{\partial U_j}{\partial x_i}\right) - \frac{2}{3}\delta_{ij}k \tag{3}$$

in which the eddy viscosity is determined as

$$\upsilon_T = C_\mu \frac{k^2}{\varepsilon} \tag{4}$$

where C_μ is an empirical constant; k is the turbulent kinetic energy; ε is the dissipation rate of turbulent kinetic energy; and δ_{ij} is Kronecker's delta.

In order to take the wall damping effect into account, $k-\varepsilon$ models for low Reynolds number flows are adopted (Patel et al., 1985), which involve empirical constants and additional terms expressed as follows:

$$\frac{\partial k}{\partial t} + U_j \frac{\partial k}{\partial x_j} = \frac{\partial}{\partial x_j}\left[\left(\frac{\upsilon_T}{\sigma_k} + \upsilon\right)\frac{\partial k}{\partial x_j}\right] - \overline{u_i' u_j'}\frac{\partial U_i}{\partial x_j} - \varepsilon \tag{5}$$

$$\frac{\partial \varepsilon}{\partial t} + U_j \frac{\partial \varepsilon}{\partial x_j} = \frac{\partial}{\partial x_j}\left[\left(\frac{\upsilon_T}{\sigma_\varepsilon} + \upsilon\right)\frac{\partial \varepsilon}{\partial x_j}\right] + C_{\varepsilon 1} f_1 \frac{\varepsilon}{k}\overline{u_i' u_j'}\frac{\partial U_i}{\partial x_j} - C_{\varepsilon 2} f_2 \frac{\varepsilon^2}{k} + E \tag{6}$$

where

$$E = 2\upsilon\upsilon_T\left(\frac{\partial^2 U}{\partial y^2}\right)^2 \tag{7}$$

Launder and Spalding (1974) recommended the following empirical constants for a fully turbulent flow, i.e. $C_\mu = 0.09$; $C_{\varepsilon 1} = 1.44$; $C_{\varepsilon 2} = 1.92$; $\sigma_k = 1.0$ and $\sigma_\varepsilon = 1.3$. Launder and Sharma (1974) proposed the following terms in the $k-\varepsilon$ model for low Reynolds number flows in boundary layers to modify the general turbulent transport equation:

$$\upsilon_T = C_\mu f_\mu \frac{k^2}{\varepsilon} \tag{8}$$

where the damping function f_μ depends on the turbulence Reynolds number R_T according to

$$f_\mu = \exp\left[\frac{-3.4}{\left(1 + R_T/50\right)^2}\right] \tag{9}$$

where

$$R_T = k^2/\upsilon\varepsilon \tag{10}$$

and

$$f_1 = 1.0,\ \ f_2 = 1 - 0.3\times\exp\left(-R_T^2\right) \tag{11}$$

III. LEVEL SET METHOD

The level set method is a numerical scheme developed to treat the evolution of interfaces and shapes. One advantage of the level set method is that one can perform numerical computations involving curves and surfaces using an Eulerian approach (with a fixed Cartesian grid). In two dimensions, the level set method represents a close curve Γ in the plane as the zero level set of a two-dimensional auxiliary function, ϕ,

$$\Gamma = \left\{ (x, y) \middle| \phi(x, y) = 0 \right\} \tag{12}$$

and then manipulates Γ implicitly through the function ϕ. This function is called a level set function. The signed distance function is generally chosen as the level set function. In this work, the interface, Γ, between air and water is the zero level set of a smoothed distance function $\phi(x, y, t)$, in which $\phi < 0$ denotes the air region and $\phi > 0$ refers to the water region. Function ϕ is defined as the signed normal distance from the interface, Γ, and satisfies $|\nabla \phi| = 1$. During time evolution, ϕ can be viewed as a property convected with the flow field. Hence,

$$\frac{\partial \phi}{\partial t} + U_j \frac{\partial \phi}{\partial x_j} = 0 \tag{13}$$

However, numerical diffusion may arise after a finite amount of computational time, i.e., the level set ϕ may become irregular and is no longer a distance function. Thus, the level set function ϕ must be re-initialized at each time step to ensure that the level set function ϕ maintains a smooth distance function. This can be achieved by iterating the following partial differential equation to reach a steady state, and then replacing $\phi(x, y, t)$ with $d(x, y, \tau)$,

$$\frac{\partial d}{\partial \tau} = S(\phi)\left(1.0 - |\nabla d| \right) \tag{14}$$

where τ is an artificial time and $S(\phi)$ is a smoothed signed function expressed as

$$S(\phi) \equiv \frac{\phi}{\sqrt{\phi^2 + |\nabla \phi|^2 \Delta^2}} \tag{15}$$

In the numerical computation, the thickness of interface, 2Δ, is chosen at least three grid cells in the direction normal to the interface, Γ. Thus, the level set function remains a distance function with $|\nabla \phi|$ converging to a unit without changing its zero level set. In numerical implementation, however, conservation of mass may be violated during the re-distancing procedure. Enright et al. (2002) developed the particle level set method to enhance the mass conservation properties of the conventional level set method and to reduce the numerical diffusion. The level set function near a free surface is adjusted by using Lagrangian marker particles.

IV. BOUNDARY AND INITIAL CONDITIONS AND NUMERICAL METHOD

Solving the RANS and turbulent transport equations requires appropriate boundary conditions at all boundaries of the solution domain, as well as the initial conditions at $t = 0$ for the entire domain. The initial conditions of velocities, hydrodynamic pressure, and surface displacement are set to zero at $t = 0$.

The kinematic condition requires that fluid particles move with the free surface. This concept can be described in terms of the advection of the level set function, as described earlier in Eq. (13). The dynamic conditions along the interface, Γ, are as follows:

$$\left. \frac{\partial \varphi}{\partial n} \right|_{\Gamma} = O \tag{16a}$$

$$P\big|_{\Gamma} = P_{atm} \tag{16b}$$

where φ denotes the mean velocity of the fluid (U or V), the turbulent kinetic energy (k), or the dissipation rate of turbulent kinetic energy (ε), and n is the direction normal to the interface, Γ, $\underline{n} = \nabla \phi / |\nabla \phi|$. Eq. (16a) can be satisfied by solving the following partial differential equation, until the steady state is achieved (Peng et al., 1999),

$$\frac{\partial \varphi}{\partial \tau} + S(\phi)\left(\frac{\nabla \phi}{|\nabla \phi|} \cdot \nabla \varphi \right) = O \tag{17}$$

where $S(\phi)$ is a smoothed signed function, as expressed in Eq. (15); τ is a fictitious time; and the operator ∇ represents $(\partial / \partial x, \partial / \partial y)$. Furthermore, the computational domain is extended with time, such that the wave does not reach the downstream boundary of the computational domain.

In the proposed numerical model, the governing equations were discretized by means of a finite-analytical scheme. The coupled velocity and pressure fields were calculated using the SIMPLER algorithm. The evolution of level set method was solved using the fourth-order TVD Runge-Kutta method and fifth-order WENO scheme. Further details on the generation of incident solitary wave in a numerical wave flume and the associated numerical schemes can be found in Huang and Dong (2001) and Dong and Huang (2004).

V. VERIFICATION

To confirm the accuracy of the incident solitary wave and the associated velocity field of the flow generated in the computational domain, Fig. 1 compares the numerical solitary

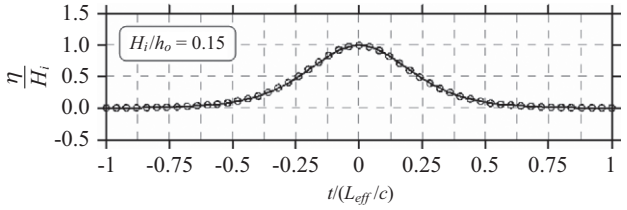

Fig. 1. Comparison of numerical solitary wave profile with that given from Boussinesq's theory; (○) Numerical results, (—) Analytical results using Boussinesq's theory.

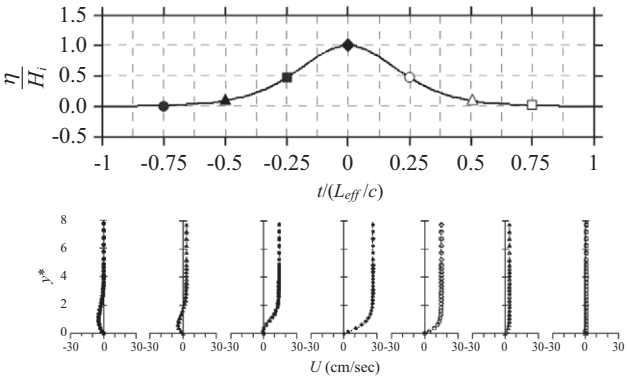

Fig. 2. Horizontal velocity profiles within the boundary layer induced by a solitary wave at different phases; (symbols) results from the proposed numerical model; (---) analytical solutions obtained from Huang and Dong (2001).

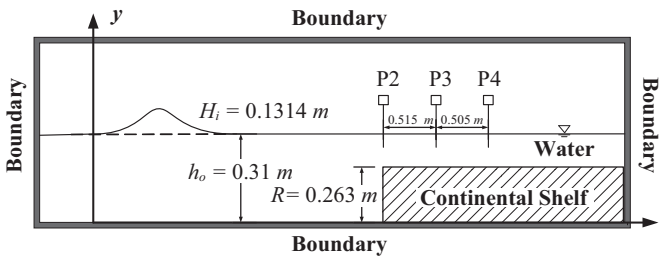

Fig. 3. Schematic diagram of the experimental setup for measuring the evolution of solitary wave over a shelf (Yasuda et al., 1997).

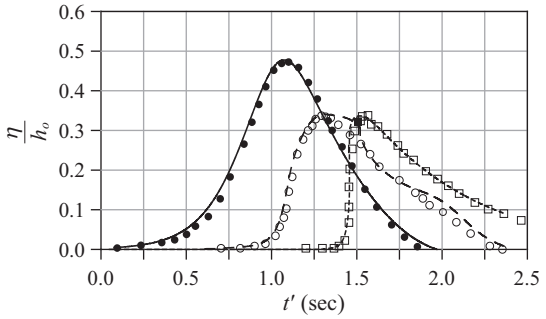

Fig. 4. Comparison between the numerical results and experimental data of the wave profile on a continental shelf; symbols (●,○, □): wave profiles recorded by the wave gauges P2 to P4, lines (—; - - -; …): numerical results; $\Delta x = \Delta y = 0.0061$.

wave profile with an incident wave height of H_i/h_o = 0.15 with the theoretical wave profile obtained from Boussinesq's theory,

$$\eta = H_i \sec h^2 \left[K(x - ct)\right] \tag{18}$$

where $K = \sqrt{3H_i / 4h_o^3}$ and c denotes the phase speed of the wave and equals to $\sqrt{g(H + h_o)}$. Additionally, h_o is the still water depth, and H_i and H denote the incident and local wave height, respectively. In Fig. 1, the time is normalized by L_{eff}/c, where L_{eff} is the effective wavelength of a solitary wave (Dean and Dalrymple, 1995).

Fig. 2 compares the numerical and theoretical horizontal velocity profiles near the bottom boundary layer induced by the solitary wave shown in Fig. 1 at different phases. The theoretical horizontal velocity profiles have been provided by Huang and Dong (2001). The numerical grids used in the computational domain are Δx = 0.1 and Δy = 0.05 except for near the wall region, where 20 and 10 grids are uniformly distributed within $0 \le y^* < 5$ and $5 \le y^* \le 10$, respectively, where y^* is defined as βy, $\beta = 0.5\sqrt{Kc/\upsilon}$. Notably, according to Figs. 1 and 2, the numerical wave profile and velocity field of the flow generated in the computational domain are accurate.

To demonstrate the accuracy of proposed numerical model in simulating breaking solitary waves on a shelf, the numerical results of the wave profile, from the incident stage to the beginning of wave overturning, are compared with the experimental data. Fig. 3 schematically depicts the experimental setup of Yasuda et al. (1997). The still water depth, h_o, is set to 0.31 *m*; the height of the shelf is 0.263 *m*; and the incident solitary wave height, H_i, is 0.1314 *m*. Four wave gauges (P1 to P4) are distributed near the leading edge of the shelf to record the temporal water surface elevation. To reduce the computational time, the numerical wave flume is set up in a finite domain of 10.5 *m* long and 0.6 *m* high using 3500 × 200 uniform computation cells. The upstream boundary condition is applied to generate the desired incident solitary wave coincident with that recorded at station P1 in the experiments, i.e. with a wave height of 0.4 h_o. The shelf is installed at 8.5 *m* (about 4 times that of the effective wave length) away from the wave paddle, and the wave probes are arranged at the same relative locations to the shelf as in Yasuda's experiments.

Fig. 4 compares the numerical and experimental water surface elevations at wave gauges P2 to P4. The time axis (t') in Fig. 4 is simply chosen to reflect the time lag when the wave crest reaches various wave gauges. The numerical results are computed with $\Delta x = \Delta y = 0.0061$. The wave gauge P4 is placed in the vicinity of the breaking point (B.P.). The lines in Fig. 4 represent the numerical results and the symbols denote the experimental data. This comparison reveals that evolution of

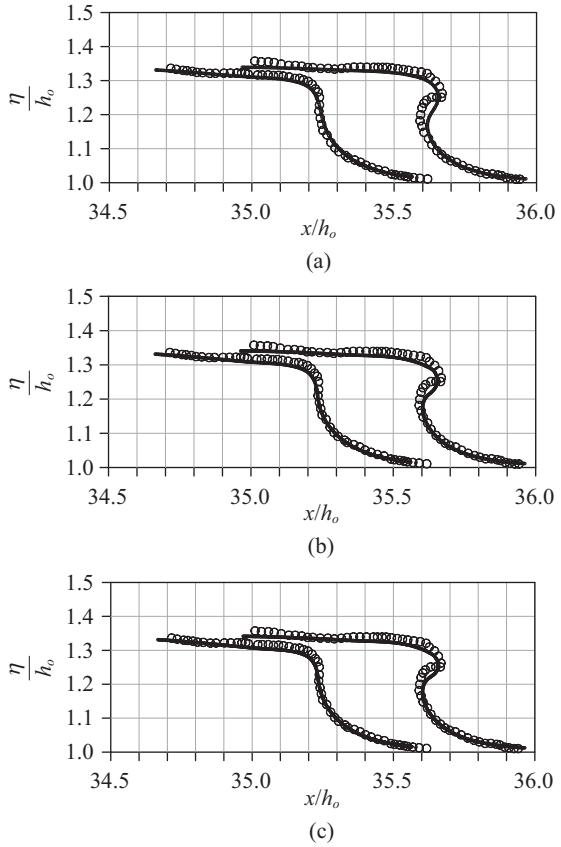

Fig. 5. Comparisons of the computed water surface profiles with the experimental records at the breaking point (left curve) and at the jet fall initiation (right curve) for various grid cell sizes; (a) $\Delta x = \Delta y = 0.0101$, (b) $\Delta x = \Delta y = 0.0061$, (c) $\Delta x = \Delta y = 0.0043$; solid line: numerical results, symbols: experimental data.

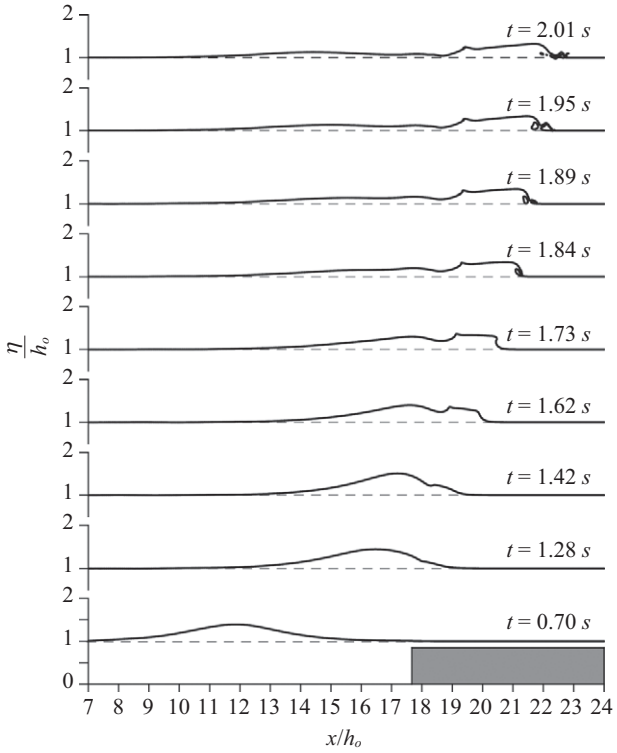

Fig. 6. Evolution of a breaking solitary wave on a shelf at different times, where $h_o = 0.31$ m, $H_i/h_o = 0.424$, $R/h_o = 0.848$.

the wave profiles from the initial incident stage to the beginning of overturning is properly simulated using this model. This comparison indicates also that before wave overturns, the grid cell size $\Delta x = \Delta y = 0.0061$ is sufficiently fine to provide an accurate resolution of the wave profiles.

Fig. 5 further compares the wave profiles after wave breaks for various grid cell sizes. With $\Delta x = \Delta y = 0.0101$ in Fig. 5(a), the grid cell sizes decrease to $\Delta x = \Delta y = 0.0061$ in Fig. 5(b), and to $\Delta x = \Delta y = 0.0043$ in Fig. 5(c). The time step Δt varies with the grid cell sizes to make the Courant number, defined as $\max(U\Delta t/\Delta x, V\Delta t/\Delta y)$, less than one. By using a high-speed video camera, Yasuda et al. (1997) obtained the spatial wave profile around the ejected jet. Two wave profiles were provided with the earlier one (i.e. the left curve) being that at the breaking point, while the latter one (i.e. the right curve) was at the beginning of the jet fall. However, Yasuda et al. (1997) did not provide the time duration between these two profiles. The numerical wave profile at the breaking point shown in Fig. 5 is identical to the experimental one, as verified in Fig. 4. Moreover, the latter one is obtained by simply choosing the one closest to the experimental data at any time. Fig. 5 indicates that with a finer grid cell size, the overturning wave profile can be properly simulated by the proposed numerical model. Additionally, the grid cell sizes in Fig. 5(b) are fine enough to capture the experimental wave profiles. Hence, in the latter computation, the grid cell sizes are set to $\Delta x = \Delta y = 0.0061$.

VI. SURFACE EVOLUTION AND KINEMATIC PROPERTIES OF FLOWS

Fig. 6 presents the evolution of the breaking solitary wave on the continental shelf from the initial incident wave at $t = 0.70$ s, to $t = 2.01$ s, when the second splash-up occurs. The incident wave conditions and geometry of the shelf in Fig. 6 are the same as those presented in Fig. 3. Fig. 6 indicates that when the solitary wave propagates over the shelf, the leading part of the wave rises due to the shoaling effect. For shallow water waves, the phase speed of the wave increases with the water depth. Hence, the bulged portion of the wave propagates at a faster speed than the front part of the wave. This propagation causes the wave to steepen towards the front, at $t = 1.73$ s, eventually toppling over at $t = 1.84$ s. This toppling effect gives rise to the typical picture of a plunging breaker. Owing to gravity, a series of splash-up occurs subsequently. Fig. 6 clearly reveals the reattachment and splash-up process of the overturning waves at $t = 1.89$ s, 1.95 s, and 2.01 s. According to Fig. 6, the proposed numerical model can elucidate complex phenomena involved in the wave breaking, such as the overturning of wave, reattachments, and splash-ups.

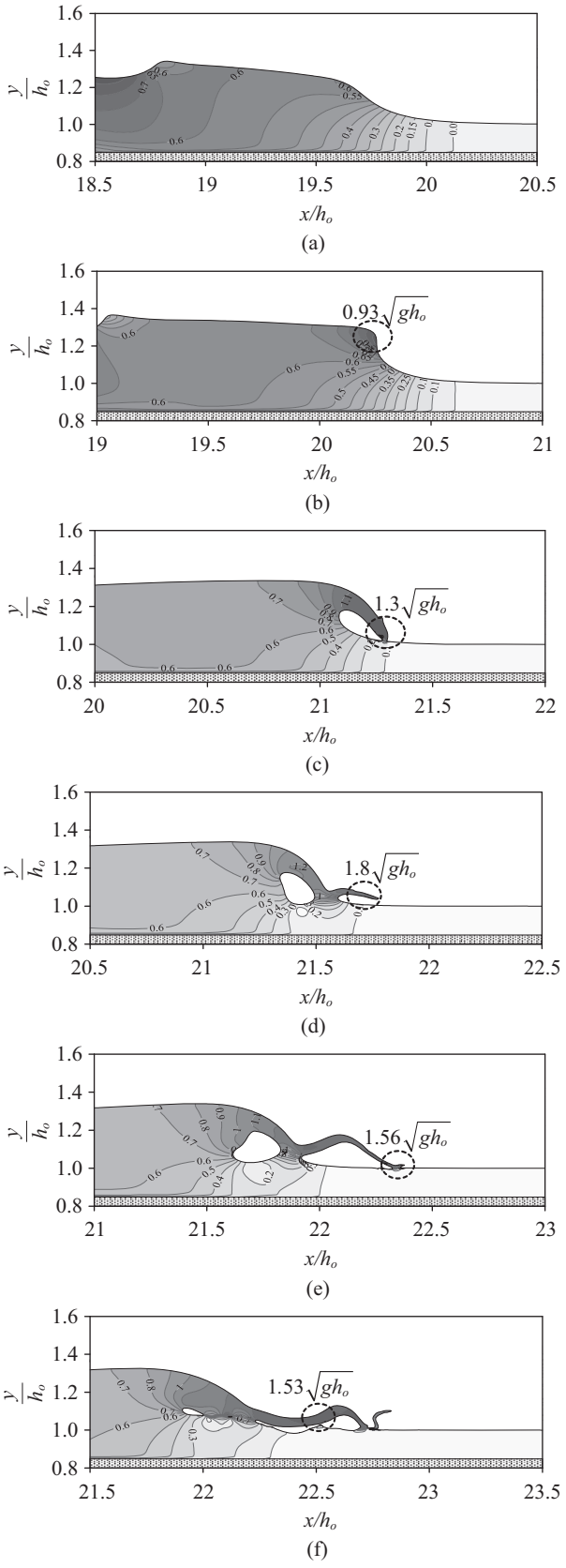

Fig. 7. Contour maps of velocities induced by a breaking solitary wave on a shelf at different times, in which t = (a) 1.62 sec, (b) 1.73 sec (c) 1.84 sec, (d) 1.89 sec, (e) 1.95 sec, and (f) 2.01 sec.

Figs. 7(a) to (f) show the contour maps of velocity fields induced by the breaking solitary wave on a shelf at different times to examine the kinematic properties of the overturning waves. In Fig. 7 the abscissas are not fixed, but are chosen to focus on the region near the front of the waves. Notably, Fig. 7 reveals that as the front of the wave evolved into a vertical shape at t = 1.73 s, Fig. 7(b), the maximum flow velocity occurs at the top of the front with a speed of 0.93 C_o (C_o = $\sqrt{gh_o}$). From t = 1.73 s to 1.84 s, water at the wave crest moves onshore gradually faster, and eventually exceeds the speed of waveform, resulting in the curling of the crest and the eventual breaking of waves. When the wave overturns and reattaches the free surface at t = 1.84 s (Fig. 7(c)), gravity seems to accelerate the ejected jet; in addition, the maximum flow velocity increases to 1.30 C_o at the leading edge of the jet. The ejected water jet then bumps against the undisturbed water surface, causing a water splash into the air, as shown in Fig. 7(d). Meanwhile, a void forms as the jet bumps into the water. The splash-up seems to receive energy from the main flow, explaining why the maximum velocity occurs at the region near the reattachment point with a high speed of 1.80 C_o, which is very close to the value of 1.68 observed by Chang and Liu (1997). Figs. 7(e) and 7(f) show the successive recurrence of the reattachment and splash-up. The fluid with the maximum velocity of 1.8 C_o in Fig. 7(d) decreases to 1.56 C_o in Fig. 7(e) and to 1.53 C_o in Fig. 7(f).

VII. ENERGY BALANCE IN A BREAKING SOLITARY WAVE ON A SHELF

The last section described the evolution of breaking solitary wave and its kinematic properties on a shelf. The physical phenomena involved in the breaking waves (e.g., reattachments, splash-ups, and air entrainment) cause energy dissipation, which is an important effect of the wave breaking and warrants further study.

Total energy of the water waves (E^{total}) can be divided into the potential energy (E^{pot}) and the kinetic energy (E^{kin}). The wave-induced potential energy can be determined as follows.

$$E^{pot} = \int_{\Omega_x}\int_{\Omega_y} H(\phi)\cdot \rho g\, y\, dy\, dx - \int_{\Omega_x}\int_0^{h_o} \rho g\, y\, dy\, dx \quad (19)$$

where Ω_x and Ω_y denote the interval of integration in the x and y axes, respectively, and h_o represents the still water depth. The kinetic energy is

$$E^{kin} = \int_{\Omega_x}\int_{\Omega_y} H(\phi)\cdot \frac{1}{2}\rho(U^2+V^2)\, dy\, dx \quad (20)$$

where U and V refer to the horizontal and vertical time-averaged mean velocity components, respectively, and $H(\phi)$ denotes the smoothed Heaviside function and is defined as

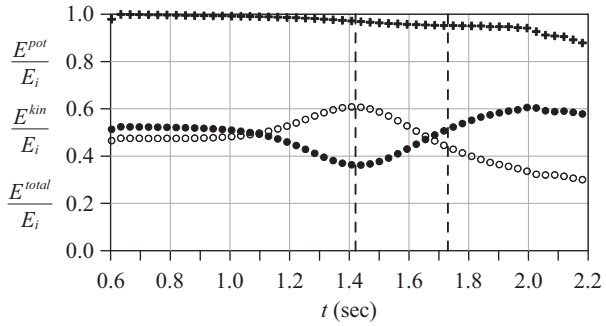

Fig. 8. Time evolutions of potential energy (○), kinetic energy (●), and total energy (+) within the whole computational domain as a solitary wave propagates over a shelf under the same conditions as those in Fig. 3.

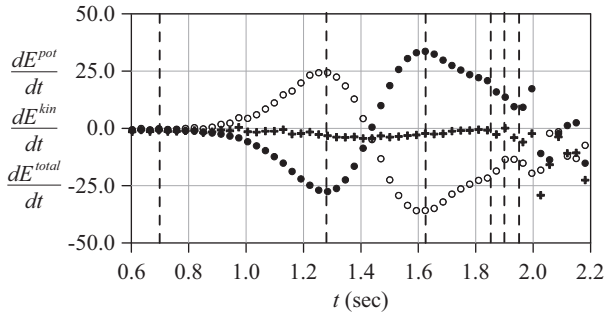

Fig. 9. Temporal variation of time rate of change of potential energy (○), kinetic energy (●), and total energy (+) as a solitary wave propagates over a shelf. The unit in the vertical axis is *Joule*/(*s*·*m*). The vertical dashed lines indicate some of the times of wave profiles shown in Fig. 6, i.e. *t* = 0.70 sec, 1.28 sec, 1.62 sec, 1.84 sec, 1.89 sec, and 1.95 sec.

$$H(\phi)=\begin{cases} O & if \quad \phi < -\Delta \\ \frac{1}{2}\left[1+\frac{\phi}{\Delta}+\frac{1}{\pi}\sin\left(\frac{\pi\phi}{\Delta}\right)\right] & if \quad -\Delta \le \phi \le +\Delta \\ 1 & if \quad \phi > +\Delta \end{cases} \tag{21}$$

Section III defines the level set function ϕ and the thickness Δ. The reflection coefficient (K_R) and transmission coefficient (K_T) are defined as

$$K_R = E^{offshore} / E_i \tag{22}$$

$$K_T = E^{onshore} / E_i \tag{23}$$

where E_i denotes the incident wave energy, and $E^{offshore}$ and $E^{onshore}$ are the energy of the wave propagating in the offshore and onshore directions, respectively. The coefficient of the energy dissipation, K_D, is then determined as follows.

$$K_D = 1 - K_R - K_T \tag{24}$$

Fig. 8 presents the time evolution of the potential energy, kinetic energy and total energy within the whole computational domain as a solitary wave propagates over a shelf under the same conditions as those in Fig. 6. Notably, Fig. 8 reveals that at the initial state, the kinetic energy of the wave is slightly larger than the potential energy. However, as the wave propagates onto the shelf, the potential energy of the wave increases gradually and reaches the maximum value at t = 1.42 s, as denoted by the first vertical dashed line. Thereafter, the potential energy decreases continuously. The decrease in the potential energy results in an increase in the kinetic energy. The total energy decreases gradually due to the energy dissipation caused by the interaction of the wave and the shelf. The second vertical dashed line in Fig. 8 denotes the time when the wave begins to break at t = 1.73 s. After the wave breaks, the potential energy decreases continuously, while the kinetic energy increases continuously due to the flow motions induced by reattachments, splash-ups, and void entrainments. However, at the latter stage, e.g., t > 2.0 s, when two reattachments and two splash-ups have occurred, all three energies decrease continuously over time.

As is widely recognized, the wave breaking is accompanied by a sudden loss of energy, although no experimental data have demonstrated this assumption yet. In Fig. 6, the wave breaking procedure begins when t > 1.73 s. According to Fig. 8, no sudden loss of wave energy is associated with the wave breaking and, in most of the procedure of wave breaking, the kinetic energy of the fluid keeps increasing, while the potential energy keeps decreasing.

To further examine the energy variation during the wave breaking, Fig. 9 displays the temporal variation of the time rate of change of the potential energy, kinetic energy, and total energy as a solitary wave propagates over a shelf. The unit in the vertical axes of Fig. 9 is $Joule/(s \cdot m)$. The vertical dashed lines in Fig. 9 indicate some of the times of the wave profiles shown in Fig. 6, i.e., t = 0.70 s, 1.28 s, 1.62 s, 1.84 s, 1.89 s, and 1.95 s. Notably, before the wave propagates onto the shelf (t < 0.9 s), the time rate of change of the three energies remains unchanged with values very close to zero. The first maximum value of the time rate of change of the potential energy appears at t = 1.28 s, corresponding to when the leading part of the wave rises due to the shoaling effect. The first maximum value of the time rate of change of the kinetic energy appears at t = 1.62 s.

Notably, after the wave overturns and reattaches the free surface at t = 1.84 s, although Fig. 8 reveals no abrupt variations in the time evolutions of the potential, kinetic, and total energy, Fig. 9 indicates that the time rate of change in the potential energy, kinetic energy and total energy significantly vary at some particular instance. For instance, after the second reattachment, which occurs at t = 1.95 s, dE^{kin}/dt increases abruptly and dE^{pot}/dt decreases rapidly. Immediately after the second splash-up, t = 2.01 s, both dE^{kin}/dt and dE^{total}/dt decline abruptly, while dE^{pot}/dt increases rapidly. Notably,

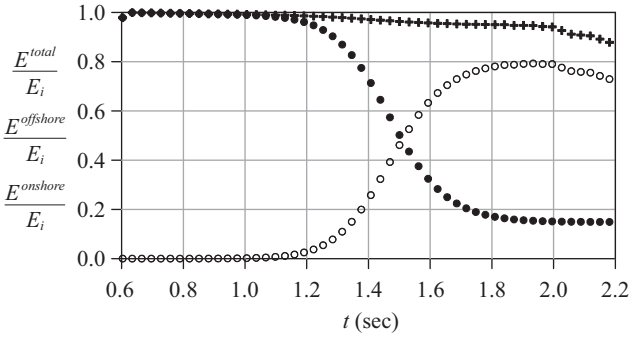

Fig. 10. Time evolution of reflected energy ($E^{offshore}/E_i$, ●), transmitted energy ($E^{onshore}/E_i$, ○), and total energy (E^{total}/E_i, +) as a solitary wave propagates over a shelf.

the maximum negative value of dE^{total}/dt appears at $t = 2.03\ s$ with a value of $-29.03\ Joule/(s \cdot m)$, after the second splash-up has occurred.

As the solitary wave propagates over the shelf, total energy of the incident wave is divided into the transmitted energy and the reflected energy. To clarify the energy loss during wave breaking, total energy is divided into two parts: the energy of the reflected wave ($E^{offshore}$) contained in the region from the wave paddle to the leading edge of the shelf ($x \cong 17.7\ h_o$), and the energy of the transmitted wave ($E^{onshore}$) above the shelf from the leading edge to the downstream of the wave tank ($x \cong 24.0\ h_o$).

Fig. 10 presents the time evolution of the reflected energy ($E^{offshore}/E_i$) and the transmitted energy ($E^{onshore}/E_i$). Initially, 100% of the total energy was evaluated in front of the shelf. As the wave propagates over the shelf, approximately 14.8% of the incident wave energy remains in front of the shelf at $t = 2.2\ s$. Thus, according to Eq. (22), the reflection coefficient K_R is 0.148. Similarly, the transmitted coefficient K_T is 0.725. Upon completion of the computation, around 87.3% of the incident wave energy remains in the computational domain. The energy dissipation involved in the whole process is then 12.7%.

Fig. 8 reveals that before wave breaking ($t < 1.73\ s$), the dissipated energy is about 5%; while at the end of computation ($t = 2.2\ s$), the totally dissipated energy increases to 12.7%. These values indicate that main part of energy dissipation occurs in the short period after wave breaks.

VIII. CONCLUSION

This work develops a numerical model to solve the unsteady two-dimensional Reynolds Averaged Navier-Stokes (RANS) equations and the $k - \varepsilon$ turbulence equations for simulating the evolution of breaking solitary waves above a shelf, or a step. The particle level set method is adopted to capture the evolving free surface, beginning from the steepening of the wave profile to the wave breaking and the successive reattachments and splash-ups. Based on the numerical results, we conclude the following.

1. Numerical results indicate that the developed numerical model can reveal the complex phenomena involved in a breaking solitary wave over a shelf, such as the overturning of wave, reattachments of the ejected jet, and splash-ups.
2. The numerical results of wave profiles near the breaking point and at the stage with an ejected jet have been shown to be identical to the experimental ones.
3. In the breaking solitary wave, the maximum local fluid velocity appears in the period between the first splash-up and the second re-attachment. The contour maps of flow velocities near the breaker front indicate that the maximum local fluid velocity is $1.8\sqrt{gh_o}$.
4. After the wave breaks, the potential energy first decreases continuously and the kinetic energy increases continuously; while at the latter stage, the potential energy seems to approach a constant value, but the kinetic energy decreases continuously in the same manner as that of the total energy.
5. Numerical results indicate that in the plunging breaking wave, both the reattachment and the splash-up are normally accompanied by an abrupt change in the time rate of change of kinetic energy (dE^{kin}/dt) and the time rate of change of potential energy (dE^{pot}/dt).

ACKNOWLEDGMENTS

The authors would like to thank the National Science Council, Taiwan, for financially supporting this research under Contract No. NSC98-2221-E-006-252 -MY3

REFERENCES

Chang, K. A. and P. L. F. Liu (1998). Velocity, acceleration and vorticity under a breaking wave. Physics of Fluids 10, 327-329.

Dean, R. G. and R. A. Dalrymple (1995). Water wave mechanics for engineers and scientists, World Scientific, Singapore.

Dong, C. M. and C. J. Huang (2004). Generation and propagation of water waves in a two-dimensional numerical viscous wave flume. Journal of Waterway, Port, Coastal, and Ocean Engineering 130, 143-153.

Enright, D., R. Fedkiw, F. Ferziger and I. Mitchell (2002). A hybrid particle level set method for improved interface capturing. Journal of Computational Physics 183, 88-116.

Goring, D. G. (1978). Tsunamis – the propagation of long waves onto a shelf. Technical Report, KH-R-38, W. M. Keck Laboratory, California Institute of Technology, Pasadena.

Huang, C. J. and C. M. Dong (2001). On the interaction of a solitary wave and a submerged dike. Coastal Engineering 43, 265-286.

Launder, B. E. and B. I. Sharma (1974). Application of the energy-dissipation model of turbulence to the calculation of flow near a spinning disc. Letters in Heat and Mass Transfer 1, 131-138.

Launder, B. E. and D. B. Spalding (1974). The numerical computation of turbulent flows. Computer Methods in Applied Mechanics and Engineering 3, 269-289.

Liu, P. L. F. and Y. Cheng (2001). A numerical study of the evolution of a solitary wave over a shelf. Physics of Fluids 13, 1660-1667.

Losada, M. A., C. Vidal and R. Medina (1989). Experimental study of the evolution of a solitary wave at an abrupt junction. Journal of Geophysical Research 94, 557-566.

Lubin, P., S. Glockner, O. Kimmoun and H. Branger (2011). Numerical study of the hydrodynamics of regular waves breaking over a sloping beach.

European Journal of Mechanics B/Fluids 30, 552-564.

Patel, V. C., W. Rodi and G. Sheuerer (1985). Turbulence models for near-wall and low Reynolds number flows: a review. AIAA Journal 23, 1308-1319.

Peng, D., B. Merriman, S. Osher, H. Zhao and M. Kang (1999). A PDE-based fast local level set method. Journal of Computational Physics 155, 410-438.

Wang, Z., Q. Zou and D. Reeve (2009). Simulation of spilling breaking waves using a two phase flow CFD model. Computers & Fluids 38, 1995-2005.

Yasuda, T., H. Mutsuda and N. Mizutani (1997). Kinematics of overturning solitary waves and their relations to breaker types. Coastal Engineering 29, 317-346.